ACS OMEGA

Open Access

http://pubs.acs.org/journal/acsodf

Article

Characterization and Mechanism Elucidation of Nano-TiO_2 Composites Prepared by Gaseous Detonation Method

Linsong Wu, Haoran Shi, Xingzhi Wang, Shiwei Lu, and Xiang Chen*

Cite This: *ACS Omega* 2024, 9, 31455−31463

Read Online

ACCESS | Metrics & More | Article Recommendations

ABSTRACT: In this study, a series of nano-TiO_2 composite materials, including nano-TiO_2, nano-SnO_2/TiO_2, nano-SiO_2/TiO_2, and nano-Fe_2O_3/TiO_2, were successfully synthesized via the gaseous detonation method. Comprehensive characterization of the synthesized samples was carried out through X-ray diffraction (XRD), transmission electron microscopy/high-resolution TEM (TEM/HRTEM), scanning electron microscopy/energy-dispersive X-ray spectroscopy (SEM/EDS), Brunauer−Emmett−Teller (BET) method, and Fourier transform infrared (FTIR) analysis, which unveiled the significant influence of precursor types on the microstructure of the composite materials. Specifically, the incorporation of Sn^{4+} promoted the transformation of TiO_2 to the rutile phase, reducing particle sizes from 25 to 19 nm and increasing the specific surface area from 44 to 86 m^2/g. In contrast, the introduction of SiO_2 impeded the rutile phase formation, leading to a marked reduction in particle size to 14 nm and an enhancement of the specific surface area to 104 m^2/g. Furthermore, the presence of Fe^{3+} promoted the formation of the rutile phase and enabled particle growth to 44 nm. These findings not only deepen the understanding of structural control in the synthesis of nano-TiO_2 composite materials via the gaseous detonation method but also highlight the critical role of precursor selection in determining the properties of the resulting materials.

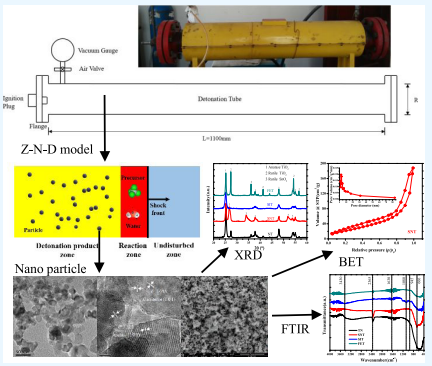

1. INTRODUCTION

TiO_2 and its composites possess exceptional redox capabilities, superior hydrophilicity, chemical stability and durability, less toxicity, and low cost.[1−3] These properties have led to extensive research and applications in areas such as hydrogen and hydrocarbon production, air and water purification, and self-cleaning, making it one of the most promising nanomaterials currently under development.[4−6]

The synthesis of nanomaterials constitutes a fundamental aspect of nanotechnology research. The choice of the preparation method significantly influences the morphological characteristics of TiO_2.[7−9] The detonation synthesis method utilizes the instantaneous characteristics of high temperature, high pressure, and high detonation speed generated during explosive detonation to prepare nanomaterials. This technique has been applied in the synthesis of nanodiamonds, nano-oxides, carbon nanotubes, and carbon-coated nanoparticles.[10−12] The gaseous detonation method represents an innovative improvement over the traditional detonation method. It utilizes combustible gases as the explosion source, eliminating the need for explosives and detonators. This method not only has a rapid reaction speed, high efficiency, and high yield but also boasts a simple reaction apparatus, low equipment requirements, low cost, and high purity. Li et al.[13] first reported the preparation of nano-TiO_2 via the gaseous detonation method. Using H_2 and air as the explosion sources and $TiCl_4$ as the precursor, a TiO_2 powder with a particle size of 10−20 nm was prepared in one step. Wu et al.[14,15] used the gaseous detonation method to prepare nano-TiO_2 composite materials and characterized their photocatalytic properties. Nepal et al.[16] used a C_2H_2−O_2 system to prepare different sizes and specific surface areas of nanographene by controlling the O_2/C_2H_2 molar ratio and discussed its industrial prospects. Dhaubhadel et al.[17] prepared silica aerosols with diameters ranging from 22 to 90 nm by detonating SiH_4 with O_2 or N_2O. Zhao et al.[18] used a hydrocarbon-O_2 system to prepare carbon-coated nanoparticles such as carbon-coated cobalt and carbon-coated copper. He et al.[19] used citric acid and urea as precursors to rapidly synthesize solid-state fluorescent carbon dots using gaseous detonation method and investigated its formation mechanism.

Researchers have conducted in-depth studies on the synthesis mechanism, influencing factors, and particle growth of nanomaterials during the gas detonation process. Yan et al.[20,21] investigated the effects of initial temperature, initial pressure, and amount of precursor on the micromorphology of nano-

Received: January 28, 2024
Revised: June 26, 2024
Accepted: July 5, 2024
Published: July 12, 2024

https://doi.org/10.1021/acsomega.4c00913
ACS Omega 2024, 9, 31455−31463

TiO_2. Wu et al.[22,23] experimentally investigated the growth mechanism of TiO_2 nanoparticles synthesized by gas detonation and established a relationship between detonation parameters and TiO_2 photocatalytic activity. Luo et al.[24,25] introduced the monodisperse Kruis model into the gaseous detonation flow field, preliminarily simulated the growth process of spherical nano-TiO_2 particles and pointed out that the reaction temperature, particle concentration, and reaction time are the main factors affecting particle growth. These studies focus more on the influence mechanism of the process parameters of the gaseous detonation method on the microstructure and properties of nanomaterials, while for gaseous detonated nano-TiO_2 composites, its microstructure and properties depend not only on the detonation parameters but also on the type of precursor. The microstructure of TiO_2 can be effectively modified by introducing different ions or compounds during the synthesis of nanocomposites. Khlyustova et al.[26] investigated the effects of Al, Cu, Mo, and W doping TiO_2 synthesized by the sol−gel method. The incorporation of these elements leads to lattice distortion of TiO_2, altering its surface characteristics and resulting in a reduction of the band gap. Ma et al.[27] doped nanonickel zinc ferrite powder with different amounts of Co^{2+}, Mn^{2+}, and Cu^{2+} using the hydrothermal method. The results showed that Co^{2+} doping could change the position of the absorption peak, enhancing the absorber's bandwidth. Mn^{2+} doping affected the lattice constant size, which decreased the wave absorption performance. Cu^{2+} doping improved the wave absorption performance. Tian et al.[28] synthesized Cu- and Fe-doped TiO_2 using the sol−gel method, demonstrating that the introduction of Cu and Fe increased the presence of lattice defects and the specific surface area of TiO_2.

In this study, we used the gaseous detonation method to prepare pure nano-TiO_2, nano-SnO_2/TiO_2 composites, nano-SiO_2/TiO_2 composites, and nano-Fe_2O_3/TiO_2 composites. And the microstructure and morphology of the samples were characterized by X-ray diffraction (XRD), transmission electron microscopy/high-resolution TEM (TEM/HRTEM), scanning electron microscope/energy-dispersive X-ray spectroscopy (SEM/EDS), Brunauer−Emmett−Teller (BET) method, and Fourier transform infrared (FTIR) analysis. The influence of different types of precursor on the crystal structure, mean particle size, specific surface area, and surface groups of the composites was investigated, which revealed the growth and phase transition mechanism of nanoparticles in gas-phase detonation reactions.

2. EXPERIMENTAL SECTION

2.1. Materials and Preparation. In this study, four different types of TiO_2 composites were investigated using $TiCl_4$ (AR, Sinopharm Group Chemical Reagent Co., Ltd.), $SnCl_4$ (AR, Sinopharm Group Chemical Reagent Co., Ltd.), $SiCl_4$ (AR, Shanghai Aladdin Reagent Co., Ltd.), and ferrocene (AR, Shanghai Aladdin Reagent Co., Ltd.) as the precursors: pure nano-TiO_2 (NT), nano-SnO_2/TiO_2 composites (SNT), nano-SiO_2/TiO_2 composites (SIT), and nano-Fe_2O_3/TiO_2 composites (FET), and the proportions of precursors for TiO_2 composites are shown in Table 1.

Sample preparation was carried out using a customized gaseous detonation tube with an inner diameter of 100 mm and a length of 1100 mm, equipped with spark plugs, gas valves, vacuum gauges, and a temperature control device, as schematically shown in Figure 1. First, the detonation tube was heated to 130 °C, then the tube was evacuated to a vacuum of −0.09 MPa using a vacuum pump, then 2 mL of precursor was injected, a certain amount of H_2 and O_2 was added, and the mixed gas was detonated after being homogeneously mixed. Finally, the powdered sample was collected.

Table 1. Experiment Parameters

no.	dosage of precursors	molar ratio	volume fraction of H_2	volume fraction of O_2	initial pressure (MPa)
NT	2.0 mL $TiCl_4$		0.1	0.8	0.1
SNT	0.4 mL $SnCl_4$	1:4.27	0.1	0.8	0.1
	1.6 mL $TiCl_4$				
SIT	0.4 mL $SiCl_4$	1:4.26	0.1	0.8	0.1
	1.6 mL $TiCl_4$				
FET	340 mg ferrocene	1:9.0	0.1	0.8	0.1
	1.8 mL $TiCl_4$				

2.2. Characterization. The sample was characterized using XRD (D/Max 2400, Cu target (Kα, wavelength λ = 0.15406), tube voltage 40 kV; tube current 30 mA; scanning speed: 8°/min; scanning step size: 0.02°/step; scanning range: 10−90°, Rigaku Corporation, Japan), TEM (Tecnai F30; acceleration voltage 300 kV; point resolution 0.2 nm; line resolution 0.1 nm; magnification 70−10mill.; FEI), FTIR (IR Affinity-1; scanning range: 4000−400 cm^{-1}; resolution: better than 0.5 cm^{-1}, wavenumber accuracy: better than 0.01 cm^{-1}; Shimadzu Corporation, Japan), SEM (NOVA NanoSEM 450; ultimate resolution 1 nm; FEI), and BET surface area analyzer (SI; Micromeritics Instrument Corporation).

3. RESULTS AND DISCUSSION

3.1. XRD Analysis. Figure 2 shows the XRD patterns of each sample, and three types of crystal structures exist in the samples: anatase TiO_2 with diffraction peaks at 2θ = 25.3, 37.9, 48.2, 54.1, and 55.2° (JCPDS No. 71−1167); rutile TiO_2 with diffraction peaks at 2θ = 27.5, 35.7, 40.9, 53.9 and 56.2° (JCPDS No. 71−0650); and rutile SnO_2 with diffraction peaks at 2θ = 26.6, 33.9, 38.0, 51.8, and 54.8° (JCPDS No. 72−1147); No crystallites containing elements of Si and Fe were found. The calculated results of each phase content and crystalline size in the samples are shown in Table 2.

NT was a mixed crystal consisting of 85% of the anatase phase with a crystallite size of 18.4 nm and 15% of the rutile phase with a crystallite size of 29.2 nm. SNT comprises 51% anatase TiO_2 and 49% rutile SnO_2. No diffraction peaks of rutile TiO_2 were detected, but comparing with the standard card revealed that the diffraction peaks of SnO_2 shifted right by 0.2°. Compared with that of NT, the rutile diffraction peak of SNT was significantly enhanced, and the amount of rutile exceeded the design value. This was due to the high structural similarity between the rutile phase of SnO_2 and that of TiO_2, as well as the similar ionic radii of Sn^{4+} and Ti^{4+} ions (0.071 and 0.068 nm, respectively). The rutile SnO_2 nuclei formed during high-temperature reactions can induce transformation of the TiO_2 crystal structure from the anatase to the rutile phase and form a solid solution. The lattice parameters in Table 2 indicate that the presence of the solid solution altered the lattice parameters and lattice spacing of the rutile phase (110), with Ti^{4+} replacing Sn^{4+} in the SnO_2 lattice.

https://doi.org/10.1021/acsomega.4c00913
ACS Omega 2024, 9, 31455−31463

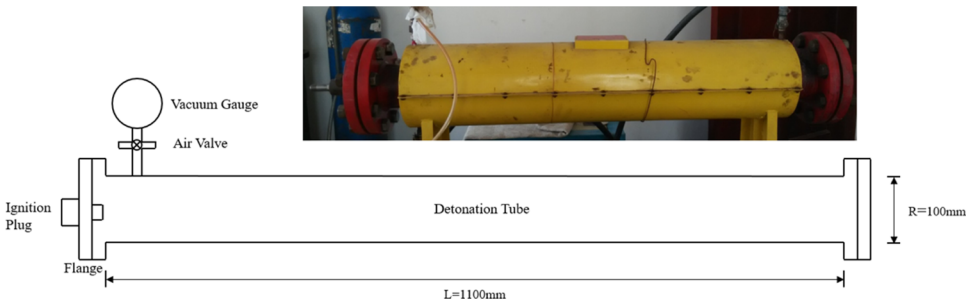

Figure 1. Schematic diagram of the detonation tube.

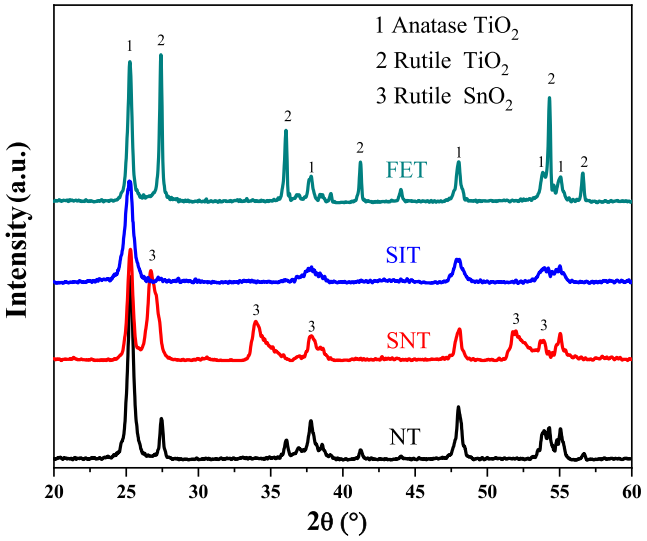

Figure 2. XRD patterns of TiO_2 composite samples.

Table 2. Particle Size, Crystal Structure, and Component Parameters of Sample

no.		NT	SNT	SIT	FET
anatase(101)	crystallite size[a] (nm)	18.4	18.7	13.6	23.0
	content (%)	85	51	100	43.7
	lattice constant *a* (Å)	3.7789	3.7820	3.7866	3.8100
	lattice constant *c* (Å)	9.5043	9.5001	9.4681	9.4463
	lattice spacing *d* (Å)	3.5180	3.5201	3.5253	3.5422
rutile(110)	crystallite size (nm)	29.2	12.1		35.0
	content (%)	15	49		56.3
	lattice constant *a* (Å)	4.5932	4.7390		4.5987
	lattice constant *c* (Å)	2.9557	3.1875		2.9678
	lattice spacing *d* (Å)	3.2396	3.3312		3.2643
mean particle size[b] (nm)		25	19	14	42
specific surface area (m^2/g)		44	86	104	67
pore volume (cm^3/g)		0.189	0.291	0.352	0.167
mean pore size (nm)		17.1	13.6	13.5	9.97
atomic ratio (X/Ti)			1:4.0	1:4.05	1:99

[a]Particle size calculated by Scherrer's formula. [b]Arithmetic mean particle size by TEM statistics.

SIT exhibits an anatase phase devoid of rutile phase diffraction peaks. Moreover, no discernible diffraction peaks corresponding to SiO_2 were detected. From Table 2, it was evident that SiO_2 doping does not significantly affect the TiO_2 lattice constants a, c, and lattice spacing d. It was reasonable to surmise that Si^{4+} does not enter the lattice of the TiO_2 anatase phase, which indicates that the presence of SiO_2 does not impact the crystal structure of TiO_2. This finding is consistent with the results of other literature.[29] This phenomenon can be attributed to the notable disparity in ionic radii between Si^{4+} (0.026−0.04 nm) and Ti^{4+} (0.068 nm), precluding the possibility of solid solution formation. Furthermore, the presence of SiO_2 hinders the transformation of TiO_2 from the anatase to rutile phase, reducing the mean particle size of the samples to 13.4 nm. FET exhibited a mixed crystal structure of anatase and rutile phases, consisting of 47.3% anatase. No diffraction peaks of Fe_2O_3 were detected. In comparison with NT, the proportion of rutile phase greatly increased, signifying that the presence of Fe^{3+} promotes the transformation of TiO_2 particles from the anatase to rutile phase. From Table 2, it was evident that Fe^{3+} doping caused a slight increase in the anatase phase lattice spacing *d* (101), while having no significant effect on the rutile phase lattice spacing *d* (110). These results imply that Fe^{3+} may replace Ti^{4+} in the lattice of anatase and generate oxygen vacancies, given the ionic radii of Fe^{3+} and Ti^{4+} at 0.065 and 0.068 nm, respectively. Gao et al. suggested that the anatase to rutile phase transition in TiO_2 was a result of Ti−O bond fracture and a synergistic interaction between Ti and O atoms, the presence of oxygen vacancies allows for atom rearrangement, promoting the transformation from anatase to rutile phase.[30]

3.2. TEM Analysis. Figure 3 presents the TEM images of each sample. NT's particle size is between 10 and 50 nm with an average of 25 nm. The particle morphology appeared spherical or spheroidal, forming chain-like agglomerates. HRTEM revealed that the (101) surface of the TiO_2 anatase phase was predominantly exposed due to its low reactivity, small surface energy, and high thermodynamic stability. It has been reported that approximately 90% of the natural anatase phase's exposed surface is the (101) surface.[31] The SNT sample exhibits a tighter particle size range of 10−40 nm, averaging around 19 nm, and shows a more uniform distribution, albeit with significant agglomeration. HRTEM analysis reveals that the main facets were TiO_2 anatase phase (101) and SnO_2 rutile phase (101). The incorporation of SnO_2 can effectively inhibit the growth of TiO_2 particles, aligning with findings from previous research.[32]

SIT's particle size was between 5 and 30 nm, with an average size of 14 nm, a finding supported by XRD analysis. This represents a notable decrease in particle size compared to that of the NT. HRTEM analysis reveals that these particles were enveloped by an amorphous SiO_2 layer that has a thickness

https://doi.org/10.1021/acsomega.4c00913
ACS Omega 2024, 9, 31455−31463

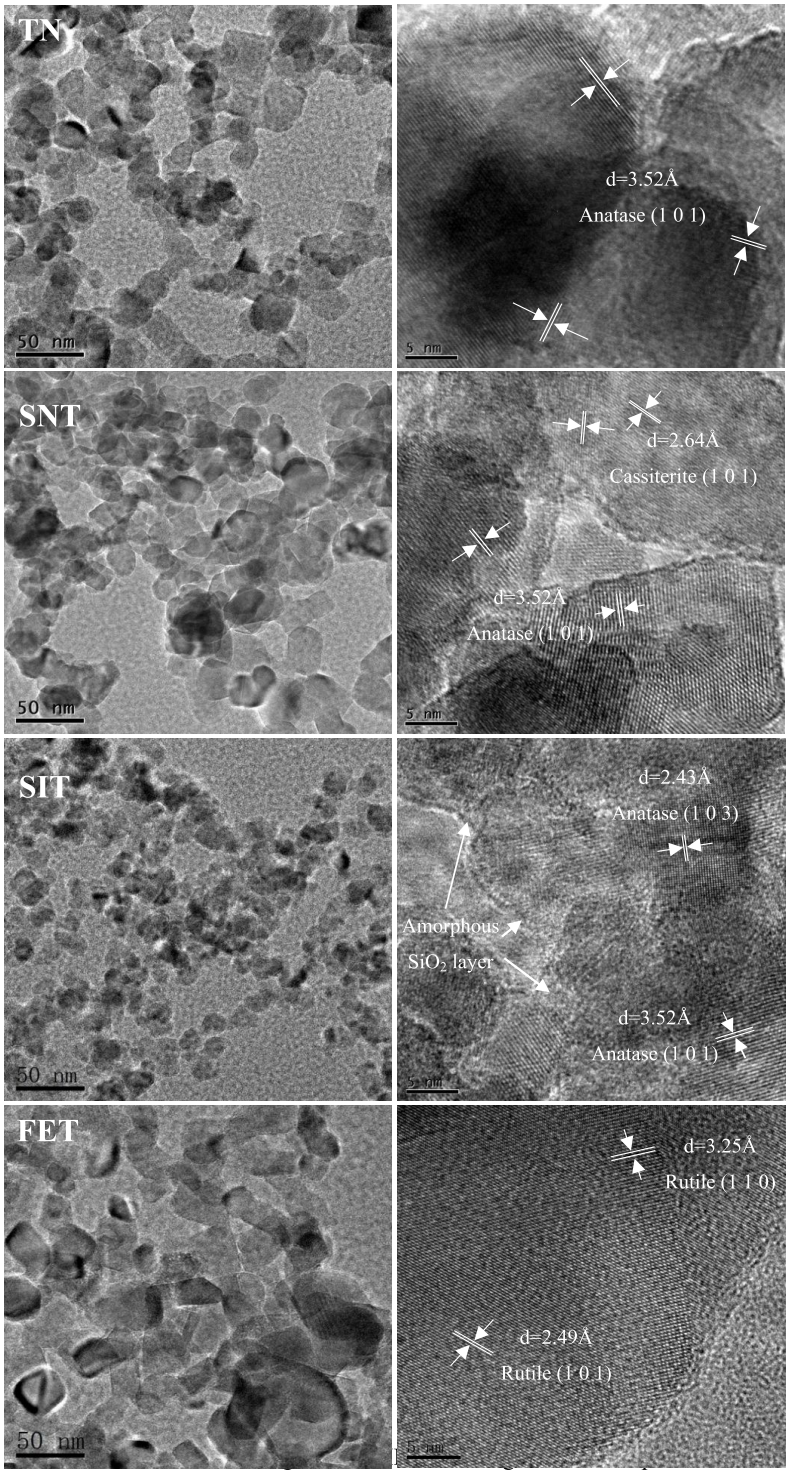

Figure 3. TEM/HRTEM images of the samples.

ranging from 0.5 to 2 nm. This is attributed to the reaction temperature in the detonation tube being about 1800 K, which is insufficient for the crystallization of nanosilica, thereby remaining amorphous within the composite material. This amorphous SiO_2 layer acts as a protective coat on the TiO_2 surface, suppressing the collision growth of the particles, improving thermal stability, and impeding phase transformation from anatase to rutile. For the FET, particle sizes were observed to range from 10 to 60 nm, with a mean particle size of 42 nm, corroborating the XRD findings. There was an observable increase in mean particle size and agglomeration level compared to that of NT, attributed to the thermal effect from the decomposition and oxidation of ferrocene. This process raises the reaction zone's temperature, accelerating TiO_2 particle growth. HRTEM analysis identified the main facets as the rutile phase TiO_2 (101), indicating a transformation influenced by the increased temperature.

3.3. BET Analysis. Figure 4 presents the N_2 adsorption−desorption isotherms and the pore size distribution curves of the samples obtained via the Barrett−Joyner−Halenda (BJH)

https://doi.org/10.1021/acsomega.4c00913
ACS Omega 2024, 9, 31455−31463

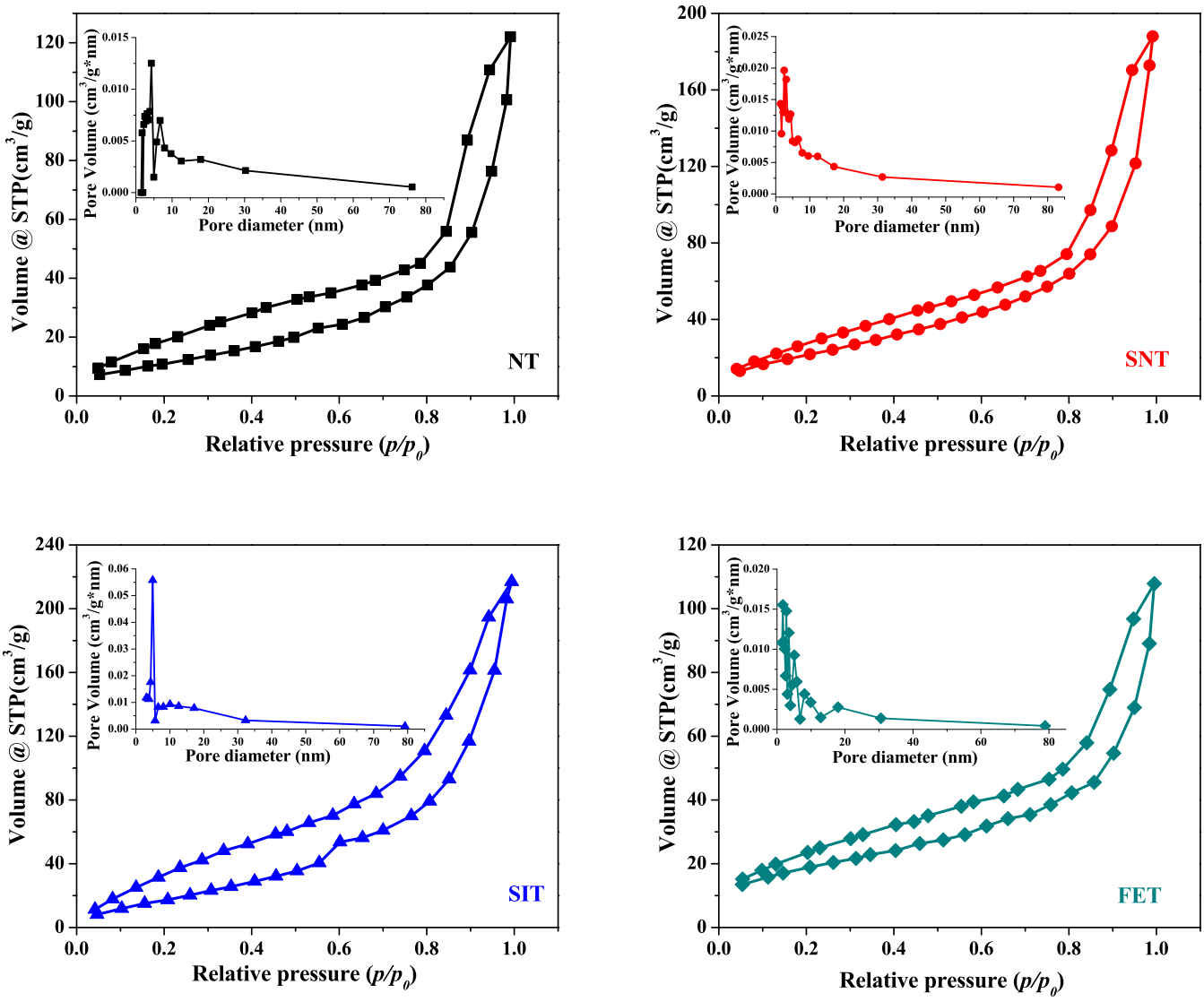

Figure 4. N_2 adsorption−desorption isotherms and the corresponding pore size distribution of the sample.

method. The structure of the adsorption−desorption isotherms of the samples were analogous, all being typical Type IV isotherms according to the IUPAC classification, which indicates that there were obvious mesoporous structures in the samples. In addition, the hysteresis loops of the adsorption−desorption isotherms of the samples were all of type H3, indicating that the pore structures of the samples were mainly slit pores formed by the accumulation of particles. The isotherms also did not exhibit signs of adsorption limits at higher relative pressures (p/p_0 = 0.99), which implied the presence of macroporous structures within the samples. Table 2 lists data on the specific surface area, pore volume, and mean pore size for the samples.

In sample NT, the mode pore size distribution ranges from 2 to 10 nm with a specific surface area of 44 m^2/g and a mean pore size of 17.1 nm. In sample SNT, the mode pore size distribution ranges from 2 to 5 nm, with a specific surface area of 86 m^2/g and a mean pore size of 13.6 nm. In sample SIT, the mode pore size distribution ranges from 2 to 5 nm, with a specific surface area of 104 m^2/g and a mean pore size of 13.5 nm. In sample FET, the mode pore size distribution ranges from 2 to 10 nm, with a specific surface area of 67 m^2/g and a mean pore size of 9.97 nm. Upon comparing these four samples, it was observed that due to identical preparation methods, the isotherm structures and hysteresis loop structures of the samples were similar. The samples also exhibit similar pore structures with micropores, mesopores, and macropores present concurrently. Samples NT, SNT, and SIT conform to the principle that smaller particle sizes correspond to larger specific surface areas. However, despite sample FET having a larger mean particle size than NT, its specific surface area was also larger than that of NT. This could be attributed to FET's more irregular particle size distribution compared to the other three samples; FET contains both small particles (10−20 nm) and large particles (50−80 nm), which aligns with TEM analysis results.

3.4. SEM/EDS Analysis. To gain a better understanding of the composite's microstructure, the samples were analyzed by SEM, as shown in Figure 5. The similar preparation method resulted in a consistent morphology for all samples, which was characterized by the aggregation of spherical particles and a homogeneous particle distribution. These findings align with the aforementioned TEM analysis. The sample particles appeared as dendritic agglomerates, and the presence of a macroporous structure formed through the connection of particle aggregates

https://doi.org/10.1021/acsomega.4c00913
ACS Omega 2024, 9, 31455−31463

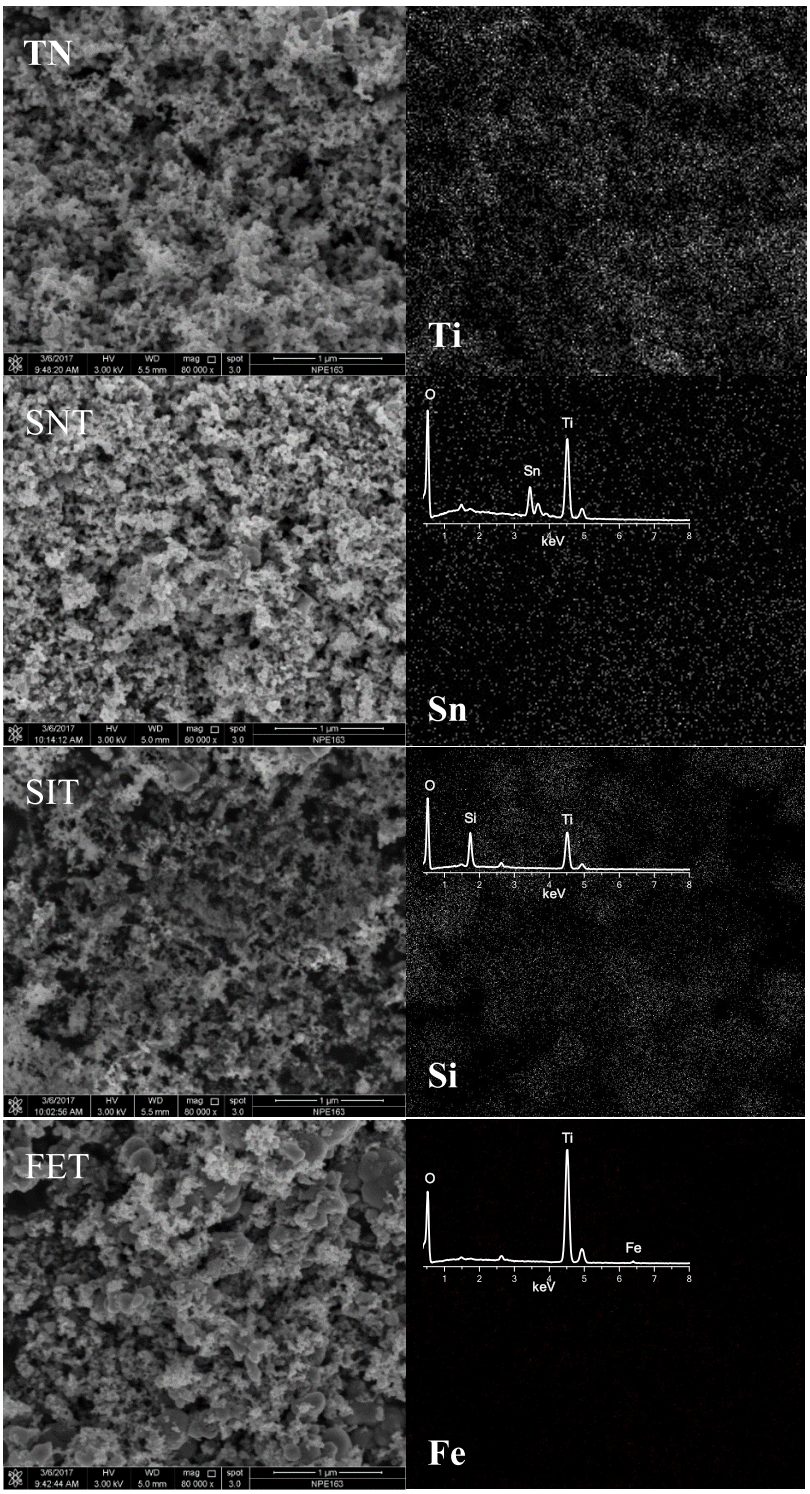

Figure 5. SEM images and EDS patterns of the samples.

and mesopore structure resulting from particle accumulation was evident. These findings align with the aforementioned BET analysis.

The distribution of elements in the analyzed samples using EDS appears in Table 2. The atomic ratio of Sn/Ti in sample SNT was 1:4, slightly higher than the design value of 1:4.27. The XRD analysis indicates that the SNT was composed of 51% anatase TiO_2 and 49% rutile SnO_2. Additionally, it confirms that the structure of the rutile phase in the SNT is not the same as that of the rutile phase of SnO_2 alone. Instead, it was a combination of the rutile phases of TiO_2 and SnO_2, forming a solid solution. The atomic ratio of Si:Ti in the SIT sample was 1:4.05, which was in line with the design value. The Fe:Ti ratio in sample FET was only 1:99, significantly deviating from the design value.

3.5. FTIR Analysis. In order to obtain the surface groups and chemical bonds of the composites, the samples were analyzed by FTIR, as shown in Figure 6. The peaks of NT around 3430 cm^{-1}

https://doi.org/10.1021/acsomega.4c00913
ACS Omega 2024, 9, 31455−31463

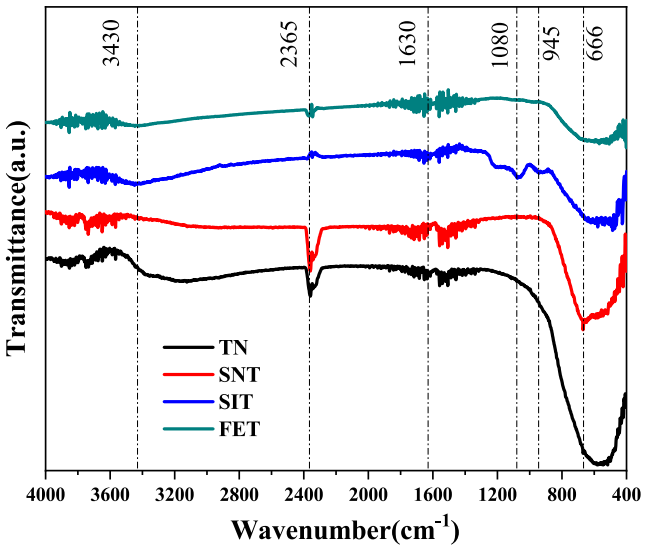

Figure 6. FTIR spectra of the samples.

exhibit the stretching vibration of −OH, resulting from hydroxyl groups or adsorbed water on the surface of TiO_2. The peaks at 2365 and 2335 cm^{-1} signify carbon dioxide's stretching vibration amidst background air, while the peaks at 1630 cm^{-1} denote the H−O−H bond's bending vibration of water adsorbed on the surface of TiO_2. The peak at 1630 cm^{-1} corresponds to the bending vibration of the H−O−H bond of adsorbed water on the surface. Surface hydroxyl groups and adsorbed water were common features of semiconductor oxides.[33] The peaks in the region near 600 cm^{-1} correspond to the telescopically recorded vibrations of Ti−O−Ti and Ti−O.

Compared with NT, the FTIR spectra of the SNT exhibited two changes. First, the Ti−O stretching vibration peak weakened, possibly due to reduced TiO_2 content in the samples. Second, the peaks shifted in the 400−700 cm^{-1} region, indicating an increase in SnO_2 content. Notably, the Sn−O stretching vibration peak appeared at around 666 cm^{-1}. Additionally, the peaks related to the Sn−O−Ti structure present in the samples were located in the 400−700 cm^{-1} region. The SNT exhibited that the Ti−O stretching vibration peak was weakened, indicating that the TiO_2 content in the sample decreases. The appearance of Ti−O−Si asymmetric stretching vibration peaks near 945 cm^{-1} and Si−O−Si asymmetric stretching vibration peaks near 1080 cm^{-1} indicates the formation of Ti−O−Si structure in the SiO_2/TiO_2 composites,[34] During the gas-phase reaction, the surface cationic vacancies on the TiO_2 transition state were filled by Si atoms, resulting in the formation of Ti−O−Si structures. This formation creates a protective layer on the TiO_2 surface, inhibiting the surface diffusion of titanium atoms, reducing collisions between TiO_2 particles, and consequently restraining the growth of the anatase-phase grains and the anatase-to-rutile phase transformation, with the previously discussed XRD analysis. In FET, the Fe−O stretching vibration peak was expected to manifest in the 480−540 cm^{-1} region; however, it was not discernible in the graph. This absence may be attributed to its potential overlap with the Ti−O absorption peak or the limited Fe_2O_3 content within the sample.

3.6. Mechanism Analysis. This study aims to investigate the influence of different precursor types on the microstructure of the composite materials. In gaseous detonation, detonation waves follow the ZND model, which exhibits a dual-layer structure: a supersonic shock wave in the front, followed by a chemical reaction zone. The shock wave serves as a significant surface of discontinuity, in which the detonation material undergoes instantaneous compression to a state with high temperature and density, followed by a chemical reaction that persists until the end of the reaction zone attains the C-J state. Precursor molecules react with water vapor under high temperatures in the reaction zone, releasing heat and further increasing the zone's temperature. Although the initial reaction mechanisms were similar across samples, variations in microstructure emerged during particle nucleation, growth, coagulation, and phase transition processes (Figure 7).

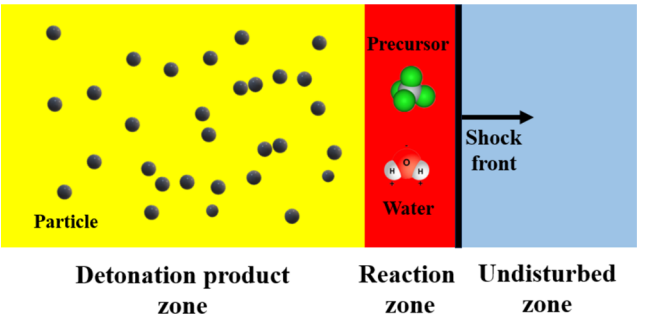

Figure 7. Schematic diagram of the Z-N-D model.

Initially, solid-phase particle nuclei precipitate for Sample NT. Nucleation and growth depend significantly on temperature, concentration, chemical equilibrium constant, and reaction rate. Primary particles then collide and coagulate into the final particles. This process decreases the number of particles and increases the particle size, which determines the final particle size and morphology. TiO_2 primary particles, initially in the anatase phase, due to the instantaneous high temperature and pressure in the detonation tube, some particles undergo a transformation into the rutile phase. In the SNT, both TiO_2 and SnO_2 solid-phase nuclei were precipitated simultaneously. The primary particles of TiO_2 were in the anatase phase, while those of SnO_2 were in the rutile phase. During the growth and coagulation of SNT, due to the high structural similarity between the rutile phases of SnO_2 and TiO_2 and the close ionic radii of Sn^{4+} and Ti^{4+} (0.071 and 0.068 nm, respectively), particles with SnO_2 primary particles as nuclei can convert to the rutile phase faster and form a solid solution. Therefore, an increase in the rutile phase content and changes in lattice parameters were observed in XRD analysis for SNT. In SIT, the primary SiO_2 particles exist in an amorphous structure. During the particle collision process, amorphous SiO_2 forms a protective layer on the surface of the TiO_2. The presence of this SiO_2 layer can hinder the collisional growth of TiO_2 particles, improve the thermal stability of TiO_2 particles, and suppress the phase transition of TiO_2 particles from anatase to rutile. This was confirmed by XRD, TEM/HRTEM, and FTIR analyses.

The reaction of the FET in the detonation tube was more complex. Its precursor, ferrocene, reacts with oxygen at high temperatures to form Fe_2O_3. Due to the large amount of heat released by this reaction, its effect on the temperature of the reaction zone cannot be ignored. Since the ionic radii of Fe^{3+} and Ti^{4+} were close (0.065 and 0.068 nm, respectively) during particle nucleation, collision, and phase transition, Ti^{4+} positions in the lattice may be replaced by Fe^{3+} to create oxygen vacancies,

https://doi.org/10.1021/acsomega.4c00913
ACS Omega 2024, 9, 31455−31463

which was beneficial for the transformation from anatase to rutile phase. In addition, an increase in the reaction zone temperature also results in a larger mean particle size for FET particles, which was reflected in XRD and TEM analyses.

4. CONCLUSIONS

In this study, we successfully prepared a series of nanocomposites, including samples NT, SNT, SIT, and FET, using the gaseous detonation method. Through comprehensive analysis and characterization of these samples, we have drawn the following key conclusions

1. Nano-SnO_2/TiO_2 consisted of 51% anatase phase, with a mean particle size of 19 nm and a specific surface area of 86 m^2/g. The presence of Sn^{4+} promotes the formation of the rutile phase of TiO_2, reducing its mean particle size by 24% and increasing its specific surface area by 95.5%.
2. Nano-SiO_2/TiO_2 was entirely in the anatase phase, with a mean particle size of 14 nm and a specific surface area of 104 m^2/g. The presence of amorphous SiO_2 hinders the formation of the rutile phase of TiO_2, reducing its mean particle size by 44% and increasing its specific surface area by 136.4%.
3. Nano-Fe_2O_3/TiO_2 consisted of 43.7% anatase phase, with a mean particle size of 42 nm and a specific surface area of 67 m^2/g. The presence of Fe^{3+} promotes the formation of the rutile phase of TiO_2, increasing its mean particle size by 68% and its specific surface area by 52.3%.
4. The type of precursor plays a key role in the crystal structure of TiO_2 composite, determining the crystal type, lattice parameters, and exposed surface of the nanocomposite particles. It significantly influences the particle size, specific surface area, and pore size of TiO_2 composite. However, it has less influence on the morphology, pore structure, and surface groups of TiO_2 composite.

In the gaseous detonation method, different precursors have a significant effect on the microstructure of TiO_2 composites, even surpassing the effect of detonation parameters on the microstructure of TiO_2 composites. Therefore, in the preparation of nano-TiO_2 composite materials, the nucleation, growth, and phase transition mechanisms of different precursors are some of the key factors in the preparation.

AUTHOR INFORMATION

Corresponding Author

Xiang Chen − *State Key Laboratory of Precision Blasting, Jianghan University, Wuhan 430056, China;* Email: chenxiang@jhun.edu.cn

Authors

Linsong Wu − *State Key Laboratory of Precision Blasting, Jianghan University, Wuhan 430056, China; School of Urban Construction, Yangtze University, Jingzhou 434023, China;* orcid.org/0000-0002-9207-9670

Haoran Shi − *School of Urban Construction, Yangtze University, Jingzhou 434023, China*

Xingzhi Wang − *School of Urban Construction, Yangtze University, Jingzhou 434023, China*

Shiwei Lu − *State Key Laboratory of Precision Blasting, Jianghan University, Wuhan 430056, China; School of Urban Construction, Yangtze University, Jingzhou 434023, China*

Complete contact information is available at: https://pubs.acs.org/10.1021/acsomega.4c00913

Notes

The authors declare no competing financial interest.

ACKNOWLEDGMENTS

This work was supported by the Open Foundation of State Key Laboratory of Precision Blasting [Grant number: BL2021-17].

REFERENCES

(1) Liao, L.; Wang, M.; Li, Z.; Wang, X.; Zhou, W. Recent Advances in Black TiO_2 Nanomaterials for Solar Energy Conversion. *Nanomaterials* **2023**, *13* (3), No. 468, DOI: 10.3390/nano13030468.

(2) Li, X.; Li, K.; Ding, D.; Yan, J.; Wang, C.; Carabineiro, S.; Liu, Y.; Lv, K. Effect of oxygen vacancies on the photocatalytic activity of flower-like BiOBr microspheres towards NO oxidation and CO_2 reduction. *Sep. Purif. Technol.* **2023**, *309*, No. 123054, DOI: 10.1016/j.seppur.2022.123054.

(3) Wu, L.; Mei, M.; Li, Z.; Liu, S.; Wang, X. Study on photocatalytic and mechanical properties of TiO_2 modified pervious concrete. *Case. Stud. Constr. Mater.* **2022**, *17*, No. e01606, DOI: 10.1016/j.cscm.2022.e01606.

(4) Wu, L.; Pei, X.; Mei, M.; Li, Z.; Lu, S. Study on Photocatalytic Performance of Ag/TiO_2 Modified Cement Mortar. *Materials* **2022**, *15* (11), No. 4031, DOI: 10.3390/ma15114031.

(5) Wang, Y.-Q.; Yang, C.; Gan, L. Preparation of direct Z-scheme Bi_2WO_6/TiO_2 heterojunction by one-step solvothermal method and enhancement mechanism of photocatalytic H_2 production. *Int. J. Hydrogen Energy* **2023**, *48* (51), 19372−19384.

(6) Liao, G.; Yao, W.; She, A. Enhanced self-cleaning capacity of RBP@TiO_2 based building coating: Synergetic effect of photocatalysis and photo-induced superhydrophilicity. *Constr. Build. Mater.* **2023**, *388*, No. 131699, DOI: 10.1016/j.conbuildmat.2023.131699.

(7) Shi, L.; Li, Z.; Ju, L.; Carrasco-Pena, A.; Orlovskaya, N.; Zhou, H.; Yang, Y. Promoting nitrogen photofixation over a periodic WS_2@TiO_2 nanoporous film. *J. Mater. Chem. A* **2020**, *8* (3), 1059−1065.

(8) Gu, S.; Liu, X.; Wang, H.; Liu, Z.; Xing, H.; Yu, L. Preparation and characterization of TiO_2 photocatalytic composites supported by blast furnace slag fibres for wastewater degradation. *Ceram. Int.* **2023**, *49* (3), 5180−5188.

(9) Dubadi, R.; Huang, S.; Jaroniec, M. Mechanochemical Synthesis of Nanoparticles for Potential Antimicrobial Applications. *Materials* **2023**, *16* (4), No. 1460, DOI: 10.3390/ma16041460.

(10) Yan, X.; He, X.; Li, X.; Wang, X.; Yan, H.; Xie, X.; Yang, J. Kinetics of inverse graphitization of detonation sintered nanodiamond/alumina composites. *Ceram. Int.* **2019**, *45* (16), 19596−19609.

(11) Du, L.; Xu, C.; Liu, J.; Lan, Y.; Chen, P. One-step detonation-assisted synthesis of Fe_3O_4-Fe@BCNT composite towards high performance lithium-ion batteries. *Nanoscale* **2017**, *9* (38), 14376−14384.

(12) Yin, H.; Chen, P.; Xu, C.; Gao, X.; Zhou, Q.; Zhao, Y.; Qu, L. Shock-wave synthesis of multilayer graphene and nitrogen-doped graphene materials from carbonate. *Carbon* **2015**, *94*, 928−935.

(13) Li, X.; Ouyang, X.; Yan, H.; Luo, N.; Mo, F. Influence of Initial Pressure on the Nano-TiO_2 Particles Synthesized by Gaseous Detonation. *Rare Met. Mater. Eng.* **2011**, *40*, 11−14.

(14) Wu, L.; Yan, H.; Xiao, J.; Li, X.; Wang, X.; Zhao, T. Characterization and photocatalytic properties of nano-Fe_2O_3-TiO_2 composites prepared through the gaseous detonation method. *Ceram. Int.* **2017**, *43* (16), 14334−14339.

(15) Wu, L.; Yan, H.; Li, X.; Wang, X. Characterization and photocatalytic properties of SnO_2-TiO_2 nanocomposites prepared through gaseous detonation method. *Ceram. Int.* **2017**, *43* (1), 1517−1521.

(16) Nepal, A.; Singh, G. P.; Flanders, B. N.; Sorensen, C. M. One-step synthesis of graphene via catalyst-free gas-phase hydrocarbon

detonation. *Nanotechnology* **2013**, *24* (24), No. 245602, DOI: 10.1088/0957-4484/24/24/245602.
(17) Dhaubhadel, R.; Rieker, T. P.; Chakrabarti, A.; Sorensen, C. M. Synthesis of Silica Aerosol Gels via Controlled Detonation. *Aerosol Sci. Technol.* **2012**, *46* (5), 596−600.
(18) Zhao, T.; Wu, L.; Wang, Z.; Yan, H.; Wang, J. One-pot rapid preparation of carbon-coated Co-Cu alloy composites via the gaseous detonation method. *J. Nanopart. Res.* **2022**, *24* (10), No. 254, DOI: 10.1007/s11051-022-05622-0.
(19) He, C.; Yan, H.; Li, X.; Wang, X. One-pot millisecond preparation of quench-resistant solid-state fluorescence carbon dots toward an efficient lubrication additive. *Diamond Relat. Mater.* **2019**, *91*, 255−260.
(20) Yan, H.; Wu, L.; Li, X.; Zhao, T. Influence of Explosion Temperature on Structure and Property of Nano-TiO_2 Prepared by Gaseous Detonation Method. *J. Inorg. Mater.* **2017**, *32* (3), 275−280.
(21) Yan, H.; Wu, L.; Li, X.; Wang, X. Optimal Design and Preparation of Nano-TiO_2 Photocatalyst Using Gaseous Detonation Method. *J. Nanosci. Nanotechnol.* **2017**, *17* (3), 2124−2129.
(22) Wu, L.; Yan, H.; Li, X.; Wang, X. Influence of $TiCl_4$ concentration on the photocatalytic performance of nano-TiO_2 synthesized by gaseous detonation. *Mater. Res. Express* **2016**, *3* (8), No. 085012, DOI: 10.1088/2053-1591/3/8/085012.
(23) Zhao, T.; Wu, L.; Wang, Z.; Yan, H. Insight on the growth mechanism of TiO_2 nanoparticles via gaseous detonation intercepting collection. *Ceram. Int.* **2023**, *49* (6), 9857−9861.
(24) Luo, N.; Jing, H.; Ma, Z.; Wang, Y.; Sung, G.; Liu, W. Growth characteristics of spherical titanium oxide nanoparticles during the rapid gaseous detonation reaction. *Particuology* **2016**, *26*, 102−107.
(25) Luo, N.; Shen, H.; Jing, H.; Ma, Z.; Yang, W. Numerical simulation of oxide nanoparticle growth characteristics under the gas detonation chemical reaction by space-time conservation element-solution element method. *Particuology* **2017**, *35*, 78−83.
(26) Khlyustova, A.; Sirotkin, N.; Kusova, T.; Kraev, A.; Titov, V.; Agagonov, A. Doped TiO_2: the effect of doping elements on photocatalytic activity. *Mater. Adv.* **2020**, *1* (5), 1193−1201.
(27) Ma, Z.; Mang, C.; Weng, X.; Zhang, Q.; Si, L.; Zhao, H. The Influence of Different Metal Ions on the Absorption Properties of Nano-Nickel Zinc Ferrite. *Materials* **2018**, *11* (4), No. 590, DOI: 10.3390/ma11040590.
(28) Tian, T.; Zhang, J.; Tian, L.; Ge, S.; Zhai, Z. Photocatalytic Degradation of Gaseous Benzene Using Cu/Fe-Doped TiO_2 Nanocatalysts under Visible Light. *Molecules* **2024**, *29*, No. 144, DOI: 10.3390/molecules29010144.
(29) Liu, Z.; Miao, Y.; Liu, M.; Ding, Q.; Tjiu, W.; Cui, X.; Liu, T. Flexible polyaniline-coated TiO_2/SiO_2 nanofiber membranes with enhanced visible-light photocatalytic degradation performance. *J. Colloid Interface Sci.* **2014**, *424*, 49−55.
(30) Gao, Q.; Wu, X.; Fan, Y. The effect of iron ions on the anatase-rutile phase transformation of titania (TiO_2) in mica-titania pigments. *Dyes Pigm.* **2012**, *95* (1), 96−101.
(31) Yu, J.; Low, J.; Xiao, W.; Zhou, P.; Jaroniec, M. Enhanced Photocatalytic CO_2-Reduction Activity of Anatase TiO_2 by Coexposed {001} and {101} Facets. *J. Am. Chem. Soc.* **2014**, *136* (25), 8839−8842.
(32) Shi, H.; Zhou, M.; Song, D.; Pan, X.; Fu, J.; Zhou, J.; Ma, S.; Wang, T. Highly porous SnO_2/TiO_2 electrospun nanofibers with high photocatalytic activities. *Ceram. Int.* **2014**, *40* (7), 10383−10393.
(33) Tseng, Y.-H.; Kuo, C.; Huang, C.; Li, Y.; Chou, P.; Cheng, C.; Wong, M. Visible-light-responsive nano-TiO(2) with mixed crystal lattice and its photocatalytic activity. *Nanotechnology* **2006**, *17* (10), 2490−2497.
(34) Kim, Y. N.; Shao, G.; Jeon, S.; Imran, S. M.; Sarawade, P. B.; Kim, H. Sol-gel synthesis of sodium silicate and titanium oxychloride based TiO_2-SiO_2 aerogels and their photocatalytic property under UV irradiation. *Chem. Eng. J.* **2013**, *231*, 502−511.

https://doi.org/10.1021/acsomega.4c00913
ACS Omega 2024, 9, 31455−31463